IMMUNOLOGY

A natural killer cell mimic against intracellular pathogen infections

Min Ge[1,2], Zesong Ruan[3], Ya-Xuan Zhu[1], Wencheng Wu[1], Chuang Yang[3]*, Han Lin[1,4]*, Jianlin Shi[1,4]*

In the competition between the pathogen infection and the host defense, infectious microorganisms may enter the host cells by evading host defense mechanisms and use the intracellular biomolecules as replication nutrient. Among them, intracellular *Staphylococcus aureus* relies on the host cells to protect itself from the attacks by antibiotics or immune system to achieve long-term colonization in the host, and the consequent clinical therapeutic failures and relapses after antibiotic treatment. Here, we demonstrate that intracellular *S. aureus* surviving well even in the presence of vancomycin can be effectively eliminated using an emerging cell-mimicking therapeutic strategy. These cell mimics with natural killer cell–like activity (NKMs) are composed of a redox-responsive degradable carrier, and perforin and granzyme B within the carrier. NKMs perform far more effectivly than clinical antibiotics in treating intracellular bacterial infections, providing a direct evidence of the NK cell–mimicking immune mechanism in the treatment of intracellular *S. aureus*.

INTRODUCTION

Staphylococcus aureus, the leading cause of bacterial infection in bodies worldwide, is a major threat to human lives (*1*). In the past decades, the emergence and rapid spread of methicillin-resistant *S. aureus* (MRSA), a kind of bacteria resistant to common clinical β-lactam antibiotics, has made the *S. aureus* infections increasingly difficult to treat (*2*). Disappointingly, the reduced susceptibility of MRSA to vancomycin has been reported in clinics (*3*). MRSA is a pathogen capable of colonizing the skin and nasal mucosa of healthy individuals (*4*). Once colonized by MRSA, patients can suffer diseases such as osteomyelitis, endocarditis, pneumonia, and sepsis (*5*, *6*). Numerous studies over the decades have illustrated that *S. aureus* is capable of invading cells and surviving thereinto, resulting in high resistance to the attacks by exogenous antibiotics or phagocytic cells, and the consequent ineffective bacterial clearance in vivo (*7*–*12*). At the same time, cellular nutrients will be used by *S. aureus*, which has been shown to reverse the innate immune response by inducing the proliferation of regulatory macrophages and even killing neutrophils (*13*–*15*). Together, these evidences suggest that the eradication of intracellular *S. aureus* to avoid recurrence is currently a major challenge in clinical infection therapy.

As one of the major bacterial pathogens, *S. aureus* is responsible for approximately 80% of all cases of human osteomyelitis, which can invade and remain within osteoblasts, making osteomyelitis a chronic and unmanageable infectious disease of bone (*16*). Resultantly, osteomyelitis shows especially low response to conventional antibiotic therapy, such as surgical debridement and antibiotic chemotherapy, due to the anatomical and physiological characteristics of bone, intracellular colonization of the bacteria, and biofilm formation on implants, leading to poor prognosis (*17*, *18*). Actually, approximately 40% of patients still suffer from recurrent and persistent infections after receiving conventional clinic treatments (*19*). Other antibiotic alternative strategies, such as hyperthermia, photodynamic therapy, and nanomedicine (*20*–*22*), are also less satisfactory due to the limited penetration depth of light, or poor specificity to infected cells, or anti-immune responses of the bacteria, rendering them ineffective in eliminating deep bone infections.

Nevertheless, in the self-protection mechanism of living organism, several immune pathways are considered to be effective in clearing bacteria from infected cells, such as cytotoxic T lymphocytes (CTL) (*23*) and natural killer (NK) cells (*24*). Most recently, artificial cells have attracted intensive attention as an alternative to natural cells, exhibiting great potentials in the development of the next generation of smart materials, autonomous micromachinery, and cell mimics, which may find applications in numbers of fields from medicine to the environment, and even in establishing novel theories about the origin of life (*25*, *26*). For example, integral biological cell imitators with cell-like structures have exhibited a number of main characteristics of living cells (*27*), while comparatively engineered materials only mimic certain physical or structural features of cells (such as surface features, shape, morphology, or some specific functions) (*28*). In addition, there have been few reports on establishing cell mimics with immune cell–related functions via nanotechnology and nanoparticle construction. The latest researches have shown that a number of therapeutic strategies with dual-targeting functions to infected cells and bacteria (*29*–*31*), as well as the design of immune mimics (*28*, *32*), are effective in destroying pathogens in infected cells. Therefore, a concept of cell mimics with NK-like activity is expected to produce notable efficacy for *S. aureus* treatments (*33*).

Here, we propose an emerging therapeutic strategy that could effectively kill intracellular *S. aureus* by a cell mimic with NK-like activity, named herein as NK cell mimics (NKMs). NKMs were constructed by loading perforin and granzyme B in modified inorganic mesoporous silica nanoparticles, which can be activated after recognizing the highly expressed redox potential microenvironment around infected cells. In brief, mesoporous silica carriers could be degraded to release perforin to perforate the membrane of infected cells and create channels for granzyme B to diffuse through and then kill infected pathogens within the cells, mimicking innate immunity of NK

[1]Shanghai Institute of Ceramics, Chinese Academy of Sciences, Research Unit of Nanocatalytic Medicine in Specific Therapy for Serious Disease, Chinese Academy of Medical Sciences, Shanghai 200050, P. R. China. [2]Department of Electrical and Electronic Engineering, The University of Hong Kong, Pokfulam Road, Hong Kong, China. [3]Department of Orthopaedics, Shanghai Sixth People's Hospital Affiliated to Shanghai Jiao Tong University School of Medicine, Shanghai 200233, P. R. China. [4]Shanghai Tenth People's Hospital, Shanghai Frontiers Science Center of Nanocatalytic Medicine, School of Medicine, Tongji University, Shanghai 200331, P. R. China. *Corresponding author. Email: yangchuang@shsmu.edu.cn (C.Y.); linhan@mail.sic.ac.cn (H.L.); jlshi@mail.sic.ac.cn (J.S.)

cells for intracellular pathogen clearance mechanisms. NKMs demonstrate remarkable treatment efficacy against vancomycin-insensitive intracellular *S. aureus* infection, based on the specific recognition mechanism of changes in redox potentials before and after osteoblast infections. Besides, NKMs evoke the immunostimulatory capacity of bacteria-infected osteoblasts and augment the host's innate and adaptive immune responses to eliminate intracellular bacterial pathogens of bone tissue. NKMs treatment also shows a strong prophylactic activity against intracellular infection relapse by inducing robust bacteria-specific memory T cell responses. This kind of cell mimics simply composed of inorganic mesoporous silica as a carrier and engineered proteases as the cargoes features the advantages of easy mass production, high biosafety, and high and sustained performances against intracellular bacterial infections, which provides an innovative strategy for anti-infection and immune response activation by immune cell mimicking, exhibiting promising prospects in future clinical translation (Fig. 1).

RESULTS

Intracellular *S. aureus* is refractory to antibiotic treatments

Intracellular survival of *S. aureus* has been recognized as a possible risk factor leading to antibiotic resistance and infection persistence in osteomyelitis (*16*). To demonstrate the in vivo osteoblast infection by *S. aureus*, we analyzed the infected bone tissue of patients who were diagnosed of chronic peri-prosthetic *S. aureus* infections via Gram staining, Giemsa staining, bio–transmission electron microscopy (TEM), and confocal laser scanning microscopy (CLSM). The results show that in all four clinical samples collected from patients with confirmed recurrent *S. aureus* infections, bacteria were observed in osteoblasts located at the bone margin sites and were around 0.5 μm in size in the high-magnification TEM images, which provides direct evidence of chronic infection of osteoblasts by *S. aureus* (figs. S1 to S5). In addition, as bone cells provide a protective niche for *S. aureus* in the presence of antibiotic treatments, we evaluated the efficacy of vancomycin that is currently used as the standard of care for MRSA bone infections against bacteria sequestered inside the human osteoblast MG63 cell line (Fig. 2F). CLSM and TEM results reveal that *S. aureus* can localize into the cytosol of MG63 cells, while the number and structure of *S. aureus* are hardly influenced by vancomycin therapy (Fig. 2, A and B, and fig. S6), and the morphology of MG63 cells shows unnoticeable change after being infected by *S. aureus* (Fig. 2B). Quantitative analysis of bacterial flow cytometry and colony-forming unit (CFU) count suggests that vancomycin has failed to kill MRSA that sequestered inside osteoblasts (Fig. 2, C and D). These results demonstrate that the clinically available classical antibiotic for MRSA was ineffective in killing intracellular *S. aureus* due to the protection by the host cells, and alternative solutions are urgently needed (Fig. 2E).

Identification of enhanced reducibility as a cellular target for intracellular infections

How to discriminate between infected and uninfected cells presents a major obstacle in developing intracellular bacterial targeting strategies. It has been reported that pathogen invasion could change the cellular redox state of innate immune cells among plants and animals (*34*–*36*). Besides, changes in redox status have been observed in virus-infected antigen-presenting cells, which is proposed as a signal conceived by $CD8^+$ T cells to discriminate between uninfected and infected cells (*37*). Inspired by this, we envisaged that the

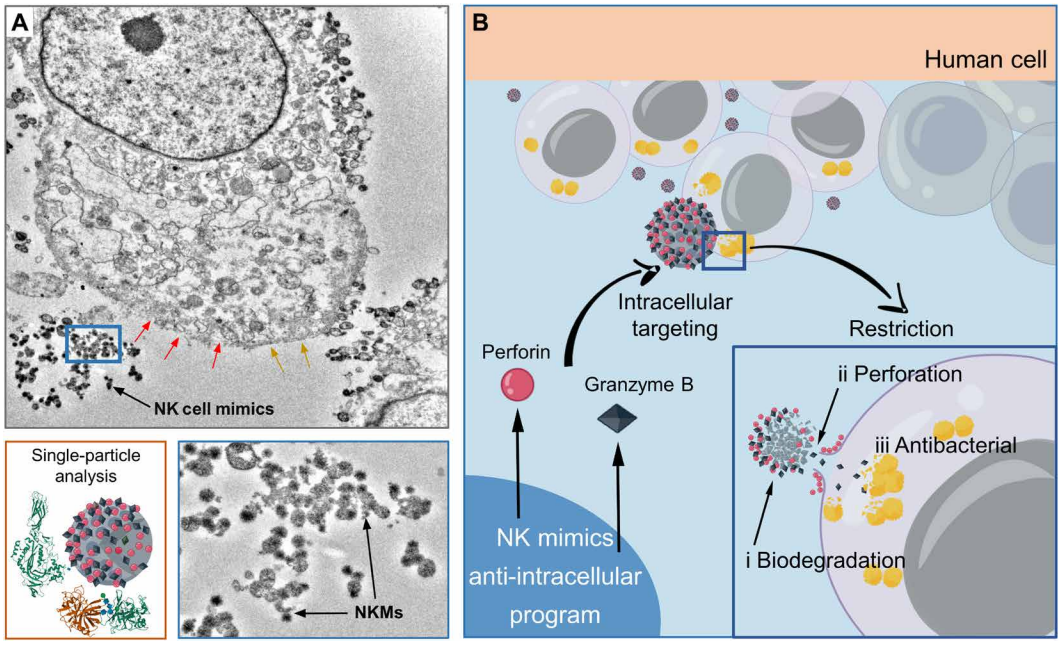

Fig. 1. NK cell mimics kill intracellular bacteria. (**A**) TEM image of NKMs (granules) added to *S. aureus*–infected osteoblast. Biodegradation of the NKMs to release perforin and granzyme B (orange border inset), triggering the disruption of the infected cell membrane (navy blue border inset). Red arrows point to damaged cell membranes with holes, and yellow arrows point to intact cell membranes. (**B**) Schematics showing that infected cells (the pale pink cells) with high redox expression induce the degradation of NKMs and the subsequent protease releases, while the oligomerization of perforin creates pores in the cell membrane, enabling the granzyme B diffusion through, which in turn targets the bacteria inside the infected cells.

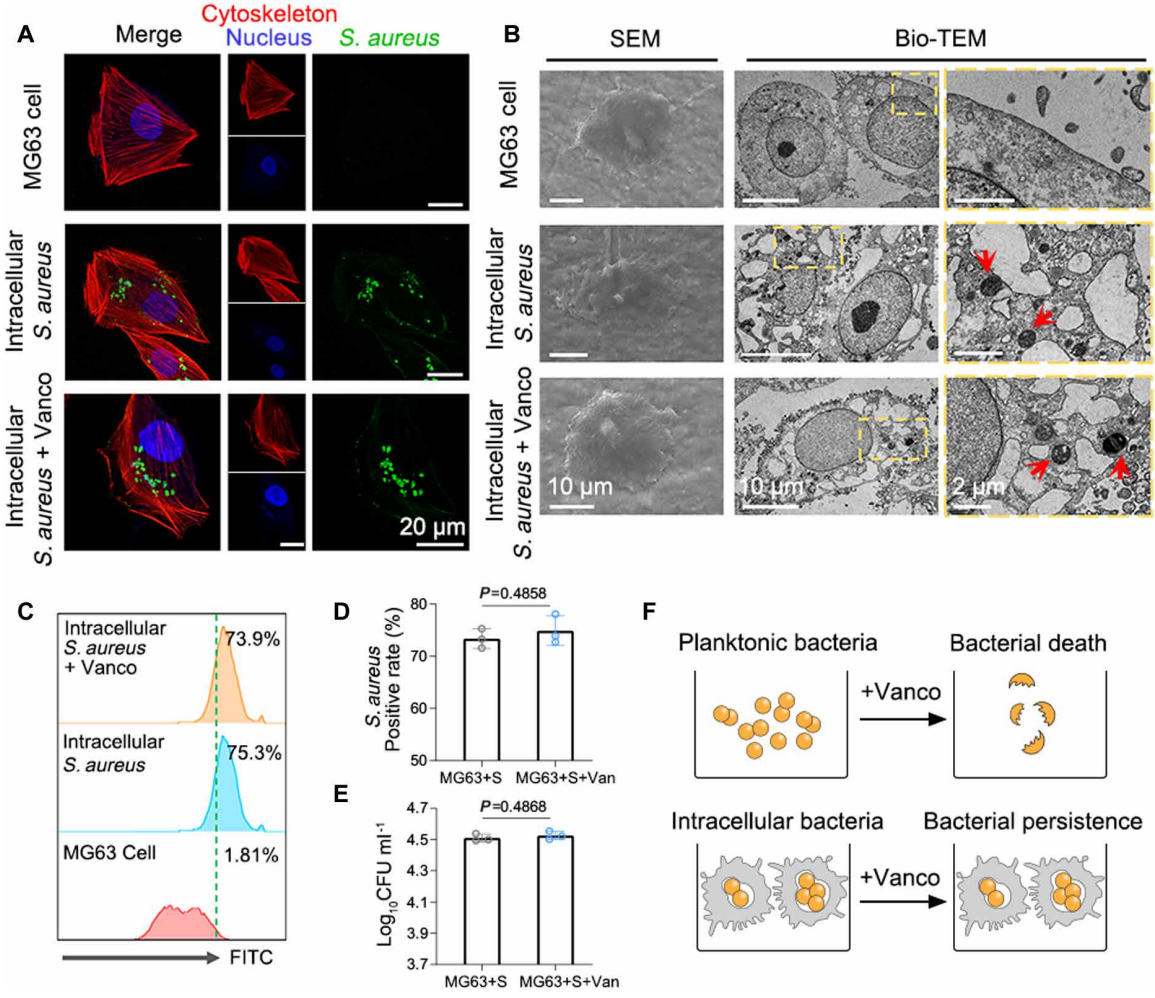

Fig. 2. Intra-osteoblastic *S. aureus* is resistant to vancomycin. MG63 cells infected with *S. aureus* were treated with or without vancomycin and imaged by (**A**) CLSM, (**B**) SEM, and bio-TEM. The red arrows indicate intra-osteoblastic *S. aureus*. (**C** and **D**) Representative flow cytometric analysis images and corresponding quantification of *S. aureus*–positive MG63 cells with or without vancomycin treatment ($n = 3$). (**E**) CFU counting of intra-osteoblastic *S. aureus* with or without vancomycin treatment ($n = 3$). (**F**) Schematic showing that intra-osteoblastic *S. aureus* is resistant to vancomycin. Data in bar graphs are presented as mean ± SD ($n = 3$), and *n* represents independent experiments. Two-tailed Student's *t* test was used for statistical analysis. Exact *P* values were provided.

redox potential of bacteria-infected cells might serve as a promising target to treat intracellular infections (Fig. 3D). We first investigate the redox-related gene expression in *S. aureus*–infected MG63 osteoblast using RNA-sequencing analysis. Hierarchical clustering reveals major divergences in nicotinamide adenine dinucleotide (NAD) pathway metabolisms between the infected and uninfected (Fig. 3A). NAD synthesis–related genes such as NAPRT and IDO are significantly up-regulated, while NAD degradation–related genes such as NNMT and PAPR are down-regulated, indicating an overall increase in oxidation-reduction metabolic activities. To monitor the reductive and oxidative status of *S. aureus*–infected MG63 osteoblast, we measured the cell surface reduction activity of infected and uninfected MG63 cells using WST-1, a membrane-impermeable regent that forms a colored product following reduction (*38*). *S. aureus*–infected MG63 osteoblasts exhibit higher cell surface reduction rates than uninfected MG63 osteoblasts (Fig. 3B). Electrochemical measurements show that MG63 cells have been infected by *S. aureus*, resulting in enhanced reducibility of the cells and decreased open circuit potential (OCP) of the working electrode due to the electron supply by the reducing species. In addition, the cyclic voltammetry (CV) results after the infection shows the intensified reduction peak, i.e., increased current density at around 30, demonstrating the promoted electron-gaining reaction (Fig. 3C). These results suggest that MG63 cells have most probably experienced certain changes in their redox species due to infection by *S. aureus* (*39*, *40*). The redox potential of a cell is mainly determined by reducible and oxidizable chemical pairs, including GSH [glutathione (reduced form)]/GSSG (oxidized glutathione), reduced thioredoxin/oxidized thioredoxin, NADH [reduced form of nicotinamide adenine dinucleotide (oxidized form) (NAD^+)]/NAD^+, and NADPH [reduced form of nicotinamide adenine dinucleotide phosphate ($NADP^+$)]/$NADP^+$ (*41*). Notably, the proportion of NADH/NAD^+, NADPH/$NADP^+$, GSH/GSSG is significantly higher for *S. aureus*–infected MG63 cells than for uninfected MG63 cells, which are responsible for the enhanced cell surface reduction rates of *S. aureus*–infected MG63 osteoblasts (Fig. 3, E to G). We expect that the increased redox activity on the

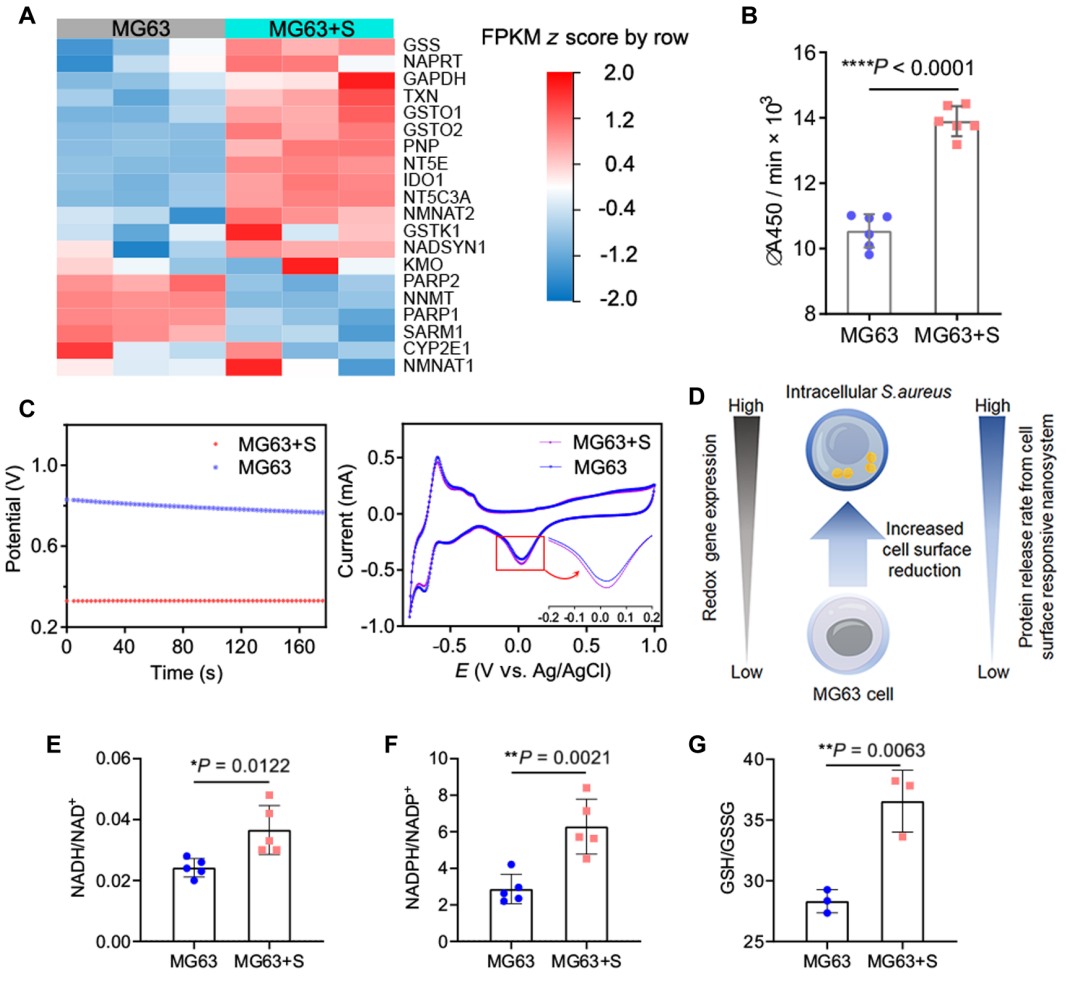

Fig. 3. *S. aureus* invasion increases cell surface reduction of host osteoblasts. (**A**) Heatmap showing hierarchical clustering of DEGs between uninfected and infected MG63 cells from three biological replicates. (**B**) Measurement of WST-1 cell surface reduction activity of *S. aureus*–infected MG63 cells in the presence of an intermediate electron acceptor. (**C**) OCP and CV curves of MG63 cells before and after being infected by *S. aureus*. (**D**) Proposed strategy for connecting increased surface redox activity of *S. aureus*–infected MG63 cells to enhanced protein release kinetics from a redox-responsive nanosystem. The proportion of (**E**) $NADH/NAD^+$, (**F**) $NADPH/NADP^+$, and (**G**) GSH/GSSG in uninfected and *S. aureus*–infected MG63 cells. Data in bar graphs are presented as mean ± SD ($n \geq 3$), and *n* represents independent experiments. Two-tailed Student's *t* test was used for statistical analysis. Exact *P* values were provided.

surface of *S. aureus*–infected MG63 osteoblasts could be used to develop an intracellular infection-specific antibacterial strategy by designing reduction-responsive nanoparticles.

Designing the NK cell mimics

These findings suggest that bacteria-infected cells exhibit a surface redox specificity, and a therapeutic modality aiming at identifying such a specificity for eliminating intracellular bacteria may be possible and promising in the prevention and treatment of intracellular pathogens. To verify this, we developed a cell-mimic therapeutic by creating an NK cell mimic that is able to be specifically activated upon the recognition of *S. aureus*–infected MG63 cells. Such NKMs were established by loading perforin and granzyme B in the mesopore channels of disulfide bond–doped dendritic mesoporous silica nanoparticles (DMONs) in the framework, followed by polyethylene glycol (PEG) modification on the DMON surface. These prepared NKMs were not directly cytotoxic to uninfected cells and will not selectively target these cells due to the unfavorable physicochemical properties based on the structural specificity of the mimics (*38*, *42*). Attractively, however, once in contact with bacterial host cells, NKMs will be cleaved by the high redox potential of the infected cell, promptly releasing perforin and granzyme B in active form. According to the properties of NK cells, we have found that more than 10 nanoparticles of NKMs can bind to a single infected cell and punch holes on the host cell membrane surface by perforin mediation, enabling sufficient amounts of granzyme B to penetrate into the phagosome to kill intracellular bacteria.

The carrier and protease in NK cell mimics played their roles in the bacteria killing. Mesoporous silica nanoparticles, a kind of typical drug delivery carrier, demonstrated high-enough biocompatibility both in vitro and in vivo (*43*–*45*). The disulfide bond–incorporated DMON nanocarriers adopted in this study can specifically degrade via the -S-S- bond breakage in response to the reducing microenvironment within cells or tumor tissues containing high concentration of GSH (*46*–*48*), leading to subsequent structural collapse for responsive load release. Here, DMON was obtained by inserting organic

groups containing disulfide bonds into the framework of mesoporous silica nanoparticles at the molecular level (fig. S7A) (*49*–*52*). Scanning electron microscopy (SEM) and TEM images reveal that the as-prepared DMONs are monodisperse and about 250 nm in diameter (Fig. 4B and fig. S7, B and C) and present a dendritic mesoporous structure. N_2 adsorption-desorption isotherms further confirm the mesoporous feature of these DMON nanoparticles, which features an average pore size of 30 nm and a Brunauer-Emmett-Teller surface area of 321.6 $m^2\ g^{-1}$ (Fig. 4E). The presence of disulfide bonds in DMON is confirmed by elemental mapping analysis (Fig. 4C), which is consistent with the energy-dispersive x-ray photoelectron spectroscopy (XPS) results (Fig. 4D and fig. S7H). To further confirm the incorporation of -S-S- bonds, DMON was characterized by ^{13}C cross-polarization magic-angle spinning (CPMAS) and ^{29}Si magic-angle spinning (MAS) solid-state nuclear magnetic resonance (NMR) spectra. From the ^{13}C NMR spectra, the peaks at 12.23, 23.88, and 42.32 ppm can be attributed to ^{1}C, ^{2}C, and ^{3}C, which correspond to the carbon atoms in the -Si-^{1}CH2-^{2}CH2-^{3}CH2-S-S-^{3}CH2-^{2}CH2-^{1}CH-Si- species, indicating the successful embedding of the organoalkoxysilane precursor bis(triethoxysilyl propyl)disulfide (BTES) within the framework of DMON (fig. S7F). In addition, the two peaks at −56.8 and −72.2 ppm in the ^{29}Si NMR spectrum are attributed to T_2 [C-Si(OSi)$_2$(OH)] and T_3 [C-Si(OSi)$_3$] species derived from BTES, while the other peaks at −100.8 and −109.9 ppm are ascribed to the Q_3 [Si(OSi)$_3$(OH)] and Q_4 [n(OSi)$_4$] species from tetraethyl orthosilicate (TEOS) (fig. S7E). In addition, the Raman spectroscopy in combination with thermogravimetry–mass spectrometry was used to demonstrate the presence of disulfide bonds. The result shows the evident release of sulfide gas from the decomposition of the organic components within DMON during heating (fig. S7G). Meanwhile,

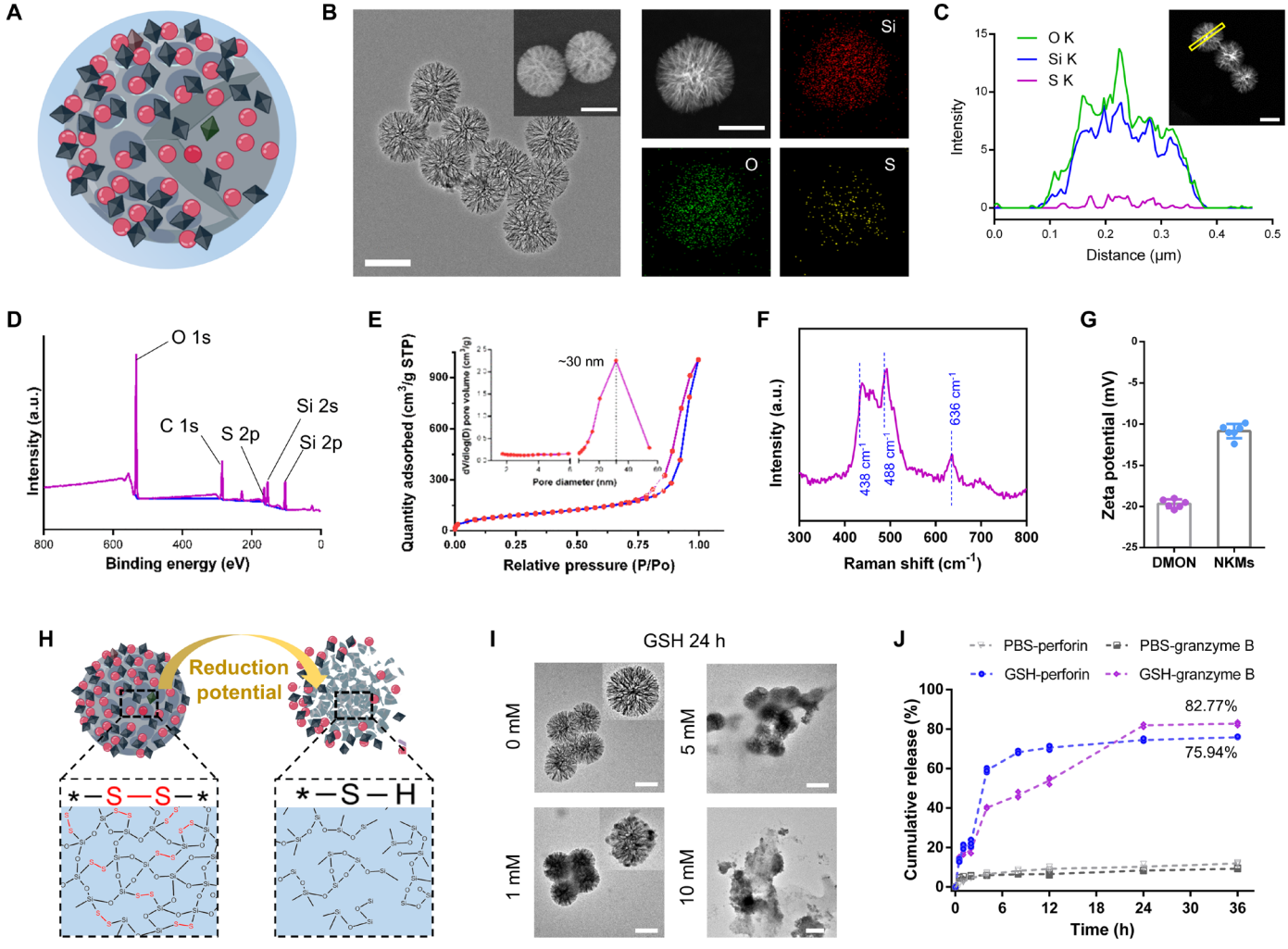

Fig. 4. Schematic and characterization of NK mimics. (**A**) Schematic showing in situ responsive NK mimics. (**B**) Representative TEM image of DMON. The inset is SEM image. The representative element-mapping images of DMON showing silicon (red), oxygen (green), and sulfur (yellow). Scale bar, 200 nm. (**C**) Linear scan element distribution of a single DMON. The inset shows the corresponding high-angle annular dark-field (HADDF) image. Scale bar, 200 nm. (**D**) XPS spectra of DMONs. (**E**) N_2 adsorption-desorption isotherms. The inset corresponds to pore-size distributions of DMON. (**F**) Raman spectrum of DMON. (**G**) Zeta potential profile of DMON and NK mimics ($n = 5$). (**H**) Schematic diagram of the release of NK mimics in the GSH environment and the change of the carrier disulfide skeleton structure. (**I**) Representative TEM images of DMON after 24 hours of incubation in GSH (0, 1, 5, and 10 mM). The inset shows the changes in the surface structure of a single nanoparticle. Scale bar, 100 nm. (**J**) Cumulative perforin and granzyme B protein release profile of NK mimics in pH 7.4 and GSH (5 mM). Data in bar graphs are presented as mean ± SD ($n \geq 3$), and n represents independent experiments.

Raman spectroscopy exhibits the specific stretching vibrations of -S-S- bonds at 437.4 and 488 cm^{-1}, and a typical stretching vibration of -S-C- bond at 636 cm^{-1} (Fig. 4F). These results suggest the successful framework hybridization of -S-C- and -S-S- bonds.

Next, the perforin and granzyme B proteins were loaded into DMON (Fig. 4A and fig. S7D) with the loading rates of 24.42% and 28.91%, respectively (fig. S7I). After loading the protease, the zeta potential of NKMs changed from −19.7 to −10.8 mV (Fig. 4G). Subsequently, the responsive degradation of DMON was investigated in reducing condition (GSH, 0, 1, 5, or 10 mM), simulating normal and different post-infection intracellular environment. NKMs exhibit a rapid degradation in the reducing condition due to the reductive cleavage of disulfide bonds (Fig. 4H). TEM images verify that DMON has completely collapsed into small fragments in the GSH solution in 24 hours. In contrast, no obvious degradation can be found in the control group in 24 hours of incubation (Fig. 4I). To verify whether the degradation of NKMs could induce the release of immobilized perforin and granzyme B, the NKM exposures in the reducing condition show a marked release of 75.94% of perforin and 82.77% of granzyme B proteins in 36 hours of incubation, which is in accordance with the DMON degradation process (Fig. 4J).

NKMs eliminate intracellular *S. aureus* in vitro

It is known that NK cells eliminate intracellular bacteria by releasing granzymes into infected cells through the pores punched by perforins (*53*). We hypothesize that NKMs could kill intracellular *S. aureus* in a similar pattern. We first investigated the capability of NKMs in killing intracellular *S. aureus* in MG63 osteoblasts. Flow cytometry assay and bacterial CFU counting reveal that NKMs can significantly reduce the intracellular *S. aureus* loads in MG63 osteoblasts (Fig. 5, B and C). Bacterial immunofluorescence staining also shows that NKM treatment eliminates intracellular *S. aureus* to a much higher degree in comparison to either DP (DMON + perforin) or DG (DMON + granzyme B) treatments (Fig. 5A and fig. S8A). In addition, CLSM images and counting results for other types of intracellular bacteria (e.g., macrophages, neutrophils, and bone marrow stromal cells) after NKM treatment show that NKMs demonstrate much improved bacterial clearance efficacy compared to the high-dose rifampicin group (*29*, *30*) owing to the advantages of its spatiotemporal sequential treatment strategy (figs. S9 to S12). Meanwhile, the cytotoxicities of NKMs themselves as well as the supernatant after the treatment of intracellular bacteria by NKMs were evaluated on various types of cells, and the Cell-Counting-Kit-8 (CCK8) results demonstrate that at the doses higher than the therapeutic concentration, NKMs as well as the inflammatory factors in the posttreatment supernatant have negligible effects on the activity of normal cells (figs. S13 and S14). These outcomes suggest that NKMs could directly play an antibacterial role in treating intracellular infections.

Subsequently, we sought to identify specific antibacterial mechanism of NKMs. We first observed intracellular *S. aureus* morphology in MG63 osteoblasts using bio-TEM and found that the border of these intracellular *S. aureus* becomes blurred upon NKM treatment (Fig. 5D). In contrast, the *S. aureus* bacteria structure inside the MG63 osteoblasts remains clear and intact upon DP and DG treatments (fig. S8B). Besides, TEM images show that NKMs have degraded upon interaction with infected MG63 osteoblasts, indicating that NKMs biodegrade in an intracellular infection-responsive manner (Fig. 5D). Alive bacteria actively acquire sulfur for bacterial protein synthesis and metabolism, while the uptake and utilization of S elements are of course no longer needed for dead bacteria (*54*, *55*). NKM treatment decreased the concentration of S element in the intracellular *S. aureus*, suggesting that NKMs have reduced intracellular bacterial viability effectively (figs. S16 and S17). In addition, pores of 10 to 60 nm in diameter can be found on the surface of *S. aureus*–infected MG63 cells due to the presence of the NKMs at the cell membrane (fig. S8D), suggesting that the perforin released from NKMs have punched pores in *S. aureus*–infected osteoblast membranes. Atomic force microscopy (AFM) images further visualize the perforation effect of NKMs, in which pores ~50 to 100 nm in diameter can be observed on the surface of *S. aureus*–infected osteoblast membranes (Fig. 5G and fig. S18, F and G). To understand the microscopic interactions between NKMs and osteoblast surfaces more clearly, we performed extensive molecular dynamic (MD) simulations for the perforation of perforin released from NKMs in the presence of lipid membranes. Notably, previous reports have demonstrated that perforins first form components of different sizes in the prepore intermediate state on the membranes of virus-infected cells and cancer cells (*56*–*59*). The prepore oligomers then become vertically collapsed in a cooperative manner, followed by insertion of subunits into the membrane to further form arc- and ring-shaped pores (*60*). In accordance with the previous findings, a clear collapsing mechanism of the oligomers has been identified in our simulations of perforin-membrane interactions (Fig. 5E). A molecular conformation with a cell membrane was constructed from 1152 1,2-dihexadecanoyl-rac-glycero-3-phosphocholine (DPPC) molecules (fig. S18, A to C), followed by further MD simulations to elucidate the effect of perforin's perforation on the cell membrane. By placing the equilibrated perforin edge above the membrane surface, we observe that the perforin-attached cellular surface exhibits strengthened morphological fluctuations of the phospholipid bilayer in the region close to the perforin (*61*, *62*) (fig. S18D). Further analysis of the height of the phospholipid bilayer confirms the formation of the pore-like pits in the area next to the perforin and phospholipid bilayer, leading to the reduced thickness of the cell membrane by approximately 25.93% on 40 ns (fig. S18E). Next, the interaction energy levels between perforin and phospholipid bilayer before and after the formation of the hole were calculated. The van der Waals interaction energy between perforin and phospholipid bilayer is −737 kJ mol^{-1}, the electrostatic interaction energy is −53 kJ mol^{-1}, and the total interaction energy is −790 kJ mol^{-1} before perforin approaches the surface of phospholipid bilayer. However, in 40 ns of perforin action on the surface of phospholipid bilayer, the van der Waals interaction energy between perforin and phospholipid bilayer reduces to −657 kJ mol^{-1}, the electrostatic interaction energy is −450 kJ mol^{-1}, and the total interaction energy is −1107 kJ mol^{-1} (Fig. 5F). The lower interaction energy of perforins with phospholipid bilayers suggests the more thermodynamically stable structure of depressed pores, manifesting the effectiveness of the spontaneous perforation through cell membranes (*63*). Notably, due to the extremely high complexity of the present system, the current computing power can only satisfy the simulation in the time framework of tens of nanoseconds; resultantly, the simulation results of multiple perforin oligomerization and the complete process of intuitive pore penetration on the cell membrane have not been obtained.

To gain more insight into the functioning mode of NKMs once in contact with mammalian cells, we used model liposomal unilamellar

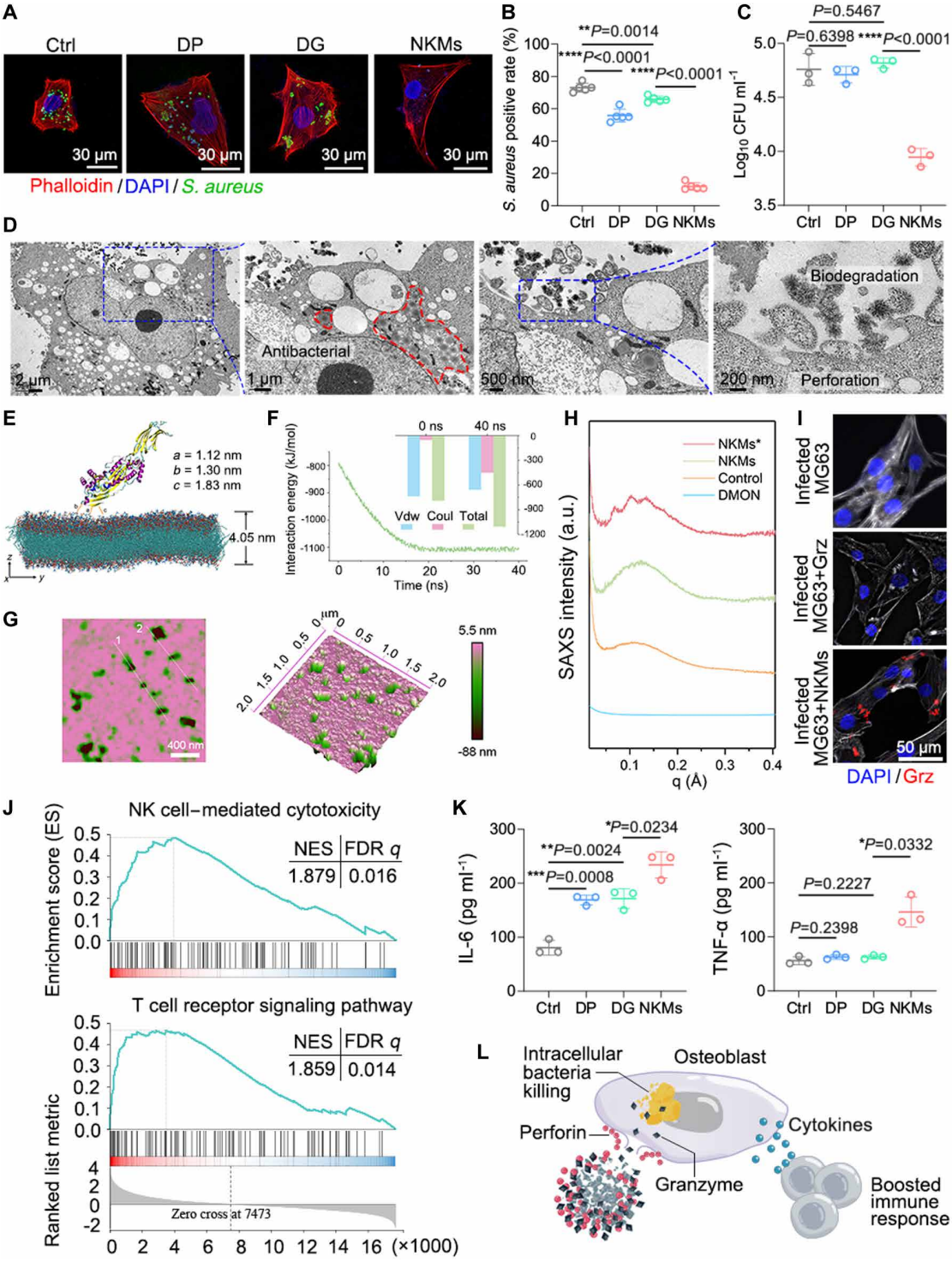

Fig. 5. Immune-like eradication of intracellular *S. aureus* by NK mimics. (**A**) CLSM images of *S. aureus*–infected MG63 osteoblast with different treatments. (**B** and **C**) Intra-osteoblastic *S. aureus* bacterial load measured by flow cytometry (B) and CFU counting (C) ($n \geq 3$). (**D**) Bio-TEM micrographs of *S. aureus*–infected MG63 osteoblast cells exposed to NKMs. Red dashed areas indicate intracellular bacteria. (**E**) Structure of perforin on the surface of a phospholipid bilayer (side view) and distance analysis to the nearest protein group in the phospholipid bilayer. (**F**) Interaction energies between perforin and phospholipid bilayers before and after pit formation. (**G**) AFM images showing the pore formation on the surface of MG63 cells exposed to NKMs. (**H**) Synchrotron SAXS of mammalian cell-mimicking liposomes after interacting with control (orange), NKMs (green), and NKMs* (red; containing the same components as NKMs, but not loaded) shows different structures. (**I**) CLSM images showing the intracellular uptake of granzyme B (Grz) by MRSA-infected MG63 cells. (**J**) GSEA pathway enrichment analysis of DEGs of infected MG63 osteoblast between the control and NKM group. (**K**) Secretion of TNF-α and IL-6 from MG63 cells after treatment with Ctrl, DP, DG, or NKMs ($n = 3$). (**L**) Schematic illustrating the intracellular bacterial killing process of NKMs and the elicitation of immunostimulating potential of osteoblast. Data in bar graphs are presented as mean ± SD ($n \geq 3$), and n represents independent experiments. Two-tailed Student's t test was used for statistical analysis. Exact P values were provided.

vesicles (LUVs) to mimic mammalian cells. Although the model liposomes are simple and partially lack the structural features of bacterial and mammalian cells, such as membrane asymmetry and the cytoskeletal network that plays an important role in endocytosis in mammalian cells (*64*), experiments performed on the model LUV still faithfully captured the basic membrane remodeling response during coincubation with NKMs (Fig. 5H). Small-angle x-ray scattering (SAXS) data show that DMON alone presents no signal, and dioleoylphosphatidylcholine (DOPC)/dioleoylphosphatidylglycerol (DOPG) membranes form vesicles only (control), while NKMs with membrane activity enable DOPC/DOPG membranes to form specific phases (*65*, *66*). As previously described, liposome-mimicking cell membranes are not redox responsive, so NKM* (with the same independent components as NKMs) is able to alter the membrane structure via perforin, inducing a membrane remodeling response and thus enhancing the characteristic peak intensity. The pore formation suggests that NKMs in contact with the cells may deliver granzyme to the infected MG63 cells. To validate this hypothesis, *S. aureus*–infected MG63 cells were investigated for possible staining by intracellular granzyme B. After the coculture with NKMs, MG63 cells were stained strongly by intracellular granzyme B. In contrast, granzyme B was barely detected in MG63 cells after coculture with DG (Fig. 5I). These results indicate that NKM-induced killing of infected target cells is dependent on perforin-enabled pore formation and granzyme delivery at the synapse; this mechanism is highly similar with the model of NK cell–mediated intracellular bacterial killing.

Although the primary roles of osteoblasts are to synthesize bone matrix, there is growing evidence that osteoblasts play an additional role in acting as nonprofessional phagocytic cells in perceiving intracellular bacterial invasion and initiating antibacterial immune responses by releasing an array of immunoregulatory molecules (*67*, *68*). To investigate whether NKMs could evoke the immune response of *S. aureus*–infected osteoblasts or not, we conducted RNA-sequencing and cytokine-releasing tests. NKM-treated *S. aureus*–infected MG63 cells exhibit a profoundly altered transcriptomic profile. Gene Set Enrichment Analysis (GSEA) analysis reveals that differentially expressed genes (DEGs) are mainly enriched in NK cell–mediated cytotoxicity and T cell receptor signaling pathway (Fig. 5J). Besides, the genes that facilitate bacterial antigen presentation and osteoblast–T cell interactions in the above pathways, such as NFKBIA, TNF, CSF2, and FYN, were up-regulated (fig. S8E). The altered gene expression suggests that NKMs may evoke the T cell–and NK cell–stimulating potential of osteoblast, thus initiating the intracellular bacterial targeted host immune responses (*69*). Cytokine-releasing test demonstrates that NKM treatment would elevate the levels of immunostimulating chemokines and cytokines such as granulocyte-macrophage colony-stimulating factor (GM-CSF), interleukin-6 (IL-6), and tumor necrosis factor–α (TNF-α), compared with DP or DG treatment (Fig. 5K and fig. S8C). Given the great potential of these inflammatory molecules in recruiting macrophages and activating T lymphocytes to boost a T helper 1 (T_H1)–type response, treatments with NKMs can greatly aid in activating host immune responses for inhibiting or even eliminating intracellular bacterial infections (*67*, *68*, *70*) (Fig. 5L).

In brief, the NKM system not only can kill intracellular bacteria like the natural NK cells but also amplifies antibacterial immune response by inducing noncanonical osteoblast immunogenicity, which further evidences the NK cell–mimicking property of the NKM system.

NKMs eliminate intracellular *S. aureus* in osteomyelitis model

Motivated by the intra-osteoblast bacteria-killing activity of NKMs observed in vitro, we examined the therapeutic potential of NKMs in murine osteomyelitis models. We first evaluated the in vivo biosafety of NKMs by analyzing routine blood and blood biochemistry, hematoxylin and eosin (H&E) and terminal deoxynucleotidyl transferase–mediated deoxyuridine triphosphate nick end labeling (TUNEL) histological staining, and Si elemental distributions of major organs at 1 week and 1 month after administration of phosphate-buffered saline (PBS), NKMs (10 mg kg^{-1}), and NKMs (20 mg kg^{-1}), respectively (figs. S19, B and C, S21, and S22). No obvious variability was observed in hematological parameters and major organ sections in NKM-treated mice. In addition, in vivo fluorescence imaging showed a strong fluorescence signal of NKMs at the site of osteomyelitis infection lesions 24 hours after administration, which was consistent with CLSM observations in tissue sections (figs. S19A and S20). Subsequently, an osteomyelitis model of *S. aureus* infection in mice was established and then NKMs were intravenously injected via the tail vein (Fig. 6, A and B). In vivo bioluminescent imaging reveals that the bacterial infection has been largely alleviated after NKM intervention, compared with the other treatments (Fig. 6C).

In osteomyelitis, the *S. aureus* invasion and survival within osteoblasts, osteoclasts, and osteocytes constitutes a possible mechanism for infection persistence and recurrence (*71*). Unfortunately, most previous studies regarding intracellular infection were performed in vitro, which are less relevant to the dynamic host-pathogen interactions in vivo. We monitored intracellular *S. aureus* infection in mouse femur bone marrow by fluorescence staining, Gram staining, and bio-TEM. As expected, NKM treatment substantially suppressed infection progression in comparison to the modest bacterial growth suppression by DP or DG treatment (Fig. 6C and fig. S23, A and B). Tissue-wide visualization of bone marrow microenvironments reveals that the bacterial load is significantly reduced after NKM treatment. High-resolution CLSM images show the colocalization of bacteria (green), nucleus (blue), and cytoskeleton (red) in the osteoblast adjacent to bone margins, indicating the prevailing intracellular presence of *S. aureus*. After the NKM therapy, we observed a remarkable reduction in intracellular bacterial burden, while DP and DG control groups maintained persistent intracellular bacterial loads (Fig. 6D). Bio-TEM also revealed typical morphology of osteoblasts infected with *S. aureus* adjacent to bone margins, which was described as an intracellular surviving form of *S. aureus* in osteomyelitis (*72*). NKM treatment has led to a substantial decrease in the residual load of intracellular *S. aureus*, compared to the control groups (Fig. 6E and fig. S23, C and D). Biofilm formation is also a major concern in osteomyelitis (*16*); thus, effective antibacterial strategies should be able to destruct biofilms for osteomyelitis treatment. SEM observation reveals that bacteria can be hardly detected on the extracted implant of mice that received NKM treatments, in stark contrast with the dense bacterial biofilm formed on the implants of control groups (fig. S23E). Meanwhile, the results of both Masson and Gram staining on days 11 and 13 demonstrate the presence of staphylococcal abscesses in the osteomyelitis model, which were clustered in the medullary cavity of the long bones and associated soft tissues, and Gram-positive *S. aureus* cells were located at the center of the abscess (*16*, *73*). The *S. aureus* abscesses were effectively eliminated after the treatment with NKMs (fig. S25). The colonization of the osteocyte lacuno-canalicular network (OLCN) by *S. aureus* is one of

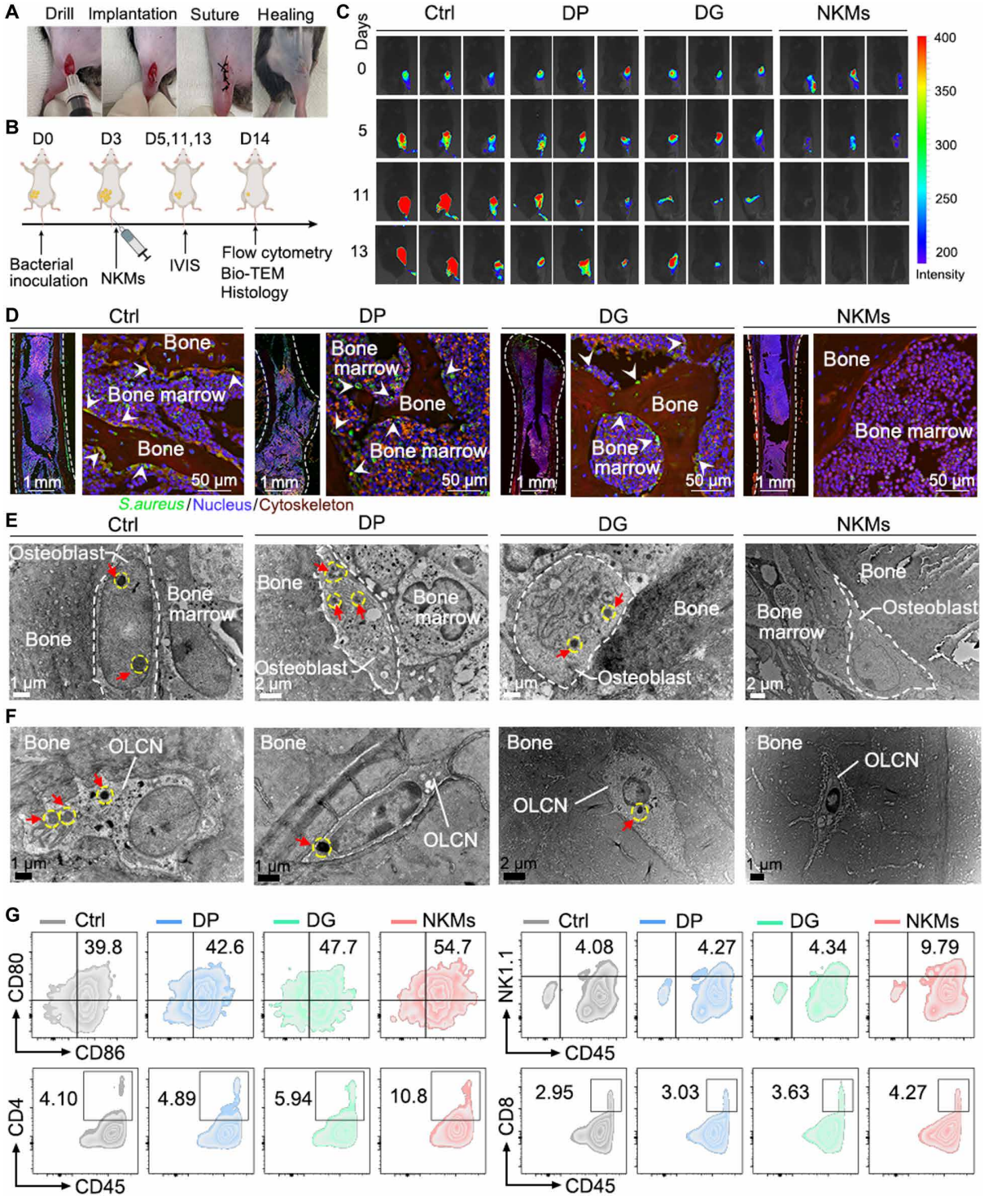

Fig. 6. NKMs eliminate intracellular *S. aureus* and evoke antibacterial immune responses in mice osteomyelitis. (**A** and **B**) Overall design of in vivo experiment. *S. aureus*–infected implants were inserted in the mice femur at the start of the experiment. At day 3, mice were allocated into four groups and DP, DG, NKMs, or PBS (10 mg kg^{-1}) was injected intravenously. Infection progression was monitors by in vivo imaging system (IVIS) imaging. (**C**) Bioluminescence imaging to monitor infection progression of osteomyelitis-bearing mice with different treatments on days 0, 5, 11, and 13 ($n = 3$ mice). (**D**) Confocal microscopy analysis of *S. aureus* and bone cells using anti–*S. aureus* antibodies (green) and phalloidin (red) in bone sections of osteomyelitis-bearing mice with different treatments. The border of bone is indicated by a white broken line, and the bacteria are indicated with white arrows. (**E**) TEM morphology of intracellular *S. aureus* in the bone sections of osteomyelitis-bearing mice with different treatments. The boundaries of osteoblasts are indicated by white dashed lines, and *S. aureus* is indicated by yellow circles and red arrows. (**F**) Intracellular morphology of *S. aureus* within OLCN locations in bone sections from osteomyelitis mice. *S. aureus* is indicated by yellow circles and red arrows. (**G**) Freshly dissected bone marrow from osteomyelitis-bearing mice with different treatments was analyzed by flow cytometry for immune composition ($n = 3$ mice). Data in bar graphs are presented as mean ± SD ($n = 3$), and *n* represents independent experiments.

the reasons for the long-term bacterial persistence of osteomyelitis and the failure of treatment, due to this unique environment that allows *S. aureus* to evade the attack by host immune cells (*74*, *75*). Bio-TEM imaging reveals the typical morphology of OLCN invaded by *S. aureus* in the infected bones (Fig. 6F). After treatment with NKMs, no obvious bacterial invasion was observed within the OLCN, suggesting that the therapeutic strategy of NKMs is effective in removing bacteria in the OLCN and may be a promising protocol as an alternative to natural immune cells in the treatment of implant-induced chronic osteomyelitis.

In addition, we evaluated the efficacy of NKMs in mouse osteomyelitis model against a cell membrane–penetrating clinical antibiotic to further highlight the clinical significance of NKMs. The results of in vivo fluorescence and bacterial enumeration show more pronounced clearance of bacteria around the implant in the high-dose rifampicin group and lower bacterial survival rate in the tissues around the site of infection than in the control group, suggesting that high-dose rifampicin has an antimicrobial effect on bacteria at the infected lesion and in the infected tissues. Comparatively, the proportion of bacteria in the infected implants and surrounding tissues is even lower in the group of mice treated with low concentrations of NKMs than with the high-dose rifampicin, suggesting that the strategy of cell-mimicking NKMs has a higher efficacy in controlling bone infections than the direct use of high-concentration, strongly cell membrane–penetrating clinically available antibiotics (fig. S26). In addition, we found that the therapeutic efficacy of NKMs is superior to the simple combination of DP and DG, confirming the necessity of a spatiotemporal "punch-bactericidal" sequential antimicrobial strategy with NKMs as cellular mimics.

On the basis of the above results, we conclude that NKMs can both kill intracellular bacteria and damage biofilms effectively (fig. S15), and both perforin and granzyme are indispensable for killing intracellular bacteria, demonstrating the attractive advantages of this NK cell–mimicking system. We also analyzed the changes in the activation status of immune cells after NKM treatment. Compared with DP or DG, NKM treatment promoted NK cell activation and dendritic cell maturation of infection-draining lymph nodes while also inducing robust bacteria-specific $CD4^+$ and $CD8^+$ T cell responses (Fig. 6G and fig. S24). We then tested the expressions of pro-inflammatory cytokines upon NKM treatment. The levels of interferon-γ (IFN-γ), GM-CSF, and TNF-α in the infection area were significantly elevated upon NKM treatment, suggesting the positive effects of NKMs on pro-inflammatory responses (fig. S23F). Among them, IFN-γ offers broad-spectrum pathogen resistance in most mammal cells through the induction of IFN-stimulated genes that encode antimicrobial factors (*76*). Together, NKMs are a highly potent immune stimulator that activates the innate and adaptive antibacterial immunity in bacteria-bearing mice. The augmented NK cell activation and cytotoxic T cell responses benefit the eradication of intracellular bacterial infections by releasing perforin and granzymes, which results in largely enhanced therapeutic efficacy of NKMs (*53*, *77*). The efficacy achieved by this synergistic strategy through the spatiotemporally controlled release of NKMs is also stronger than that of multiple doses of antibiotics and the combined administration of antibiotics and DP (figs. S31 to S33). Additionally, we did not observe any noticeable signs of tissue damage in the heart, lung, liver, kidney, or spleen, as well as body weight after NKMs treatment (figs. S23G and S34), indicating high biosafety of NKMs therapy. To exclude potential damage to the bone elicited by the boosted immune responses, bone morphology by Masson, van Gieson, Safranin O/fast green, and TUNEL staining was characterized. We observed no notable pathological osteolysis, abnormal bone remodeling, or chondral and subchondral bone damage after NKM treatments compared to control groups (figs. S25 and S27). Overall, NKM therapy exhibits safe and potent antibacterial efficacy and induces robust antitumor immune responses toward intracellular bacteria in osteomyelitis model.

NKMs trigger durable immune memory responses to prevent infection recurrence

Infection relapse is a major clinical sign of intracellular *S. aureus* infection of osteomyelitis (*78*). To determine whether NKMs would trigger long-term protective immunity or not, we challenged surviving mice with a second injection of *S. aureus* 3 months after the initial bacterial challenge and NKM treatments (Fig. 7A). The initial NKM treatments resulted in a significant reduction in the number of viable bacteria recovered from the implants and peri-implant tissues 14 days after bacterial rechallenge (Fig. 7B). H&E and Giemsa staining of infected bone samples reveal substantial neutrophil and bacterial infiltration, signs of osteomyelitis, in control groups. Comparatively, treatment with NKMs resulted in improved pathological parameters (Fig. 7, C and D). SEM observation shows that bacteria will adhere to bone marrow cells, indicating preferential invasion of the bacteria to find intracellular niche (Fig. 7E). Flow cytometric analysis shows that NKM therapy vigorously expands $CD44^{high}CD62L^{low}$ effector memory phenotypes and $CD8^+$ effector T cell subsets (Fig. 7, F to H), which could clear up bacteria once they invade the cells (*79*, *80*). To avoid interference of immune effects from residual bacteria, immune effects were also evaluated in uninfected mice and in mice reinfected after clinical antibiotic treatment (figs. S28 and S29). The above results demonstrate the indispensable role of NKMs in priming progressive bacteria-specific vaccination to resist infection relapse in osteomyelitis.

DISCUSSION

Biofilm formation and intracellular invasion are two typical features of *S. aureus* that make it a prevalent and hard-to-treat infection in human osteomyelitis (*16*). Such an intracellular survival of *S. aureus* could be one of the major mechanisms of its resistances to the intravenous antibiotics as well as the host defenses such as engulfment by white cells (*81*). NK cell is known to kill intracellular bacteria by selectively transferring antimicrobial granzymes into infected cells via the nanotubes formed by perforin (*53*). However, the clinical translation of NK cell–based immunotherapy has remained challenging, at least in part due to the difficulty in NK cell isolation, high cost, and systemic toxicities (*82*). To address this clinical challenge, we have developed herein an NK cell–mimicking platform that can be specifically activated upon interaction with *S. aureus*–infected osteoblast and kill the intracellular *S. aureus* (Fig. 1).

The present NK-mimicking platform features three biological findings. First, osteoblast will present increased cell surface reducibility following *S. aureus* intracellular invasion. The mechanisms underlying this redox regulation are most probably associated with the altered expressions of NAD synthesis and degradation-related enzymes (Fig. 3). Second, the perforin and granzyme releases from the NKM platform are essentially driven by the increased cell surface reducibility of the infected cells. Our in vitro studies have well revealed the NKM biodegradation and the perforation and granzyme

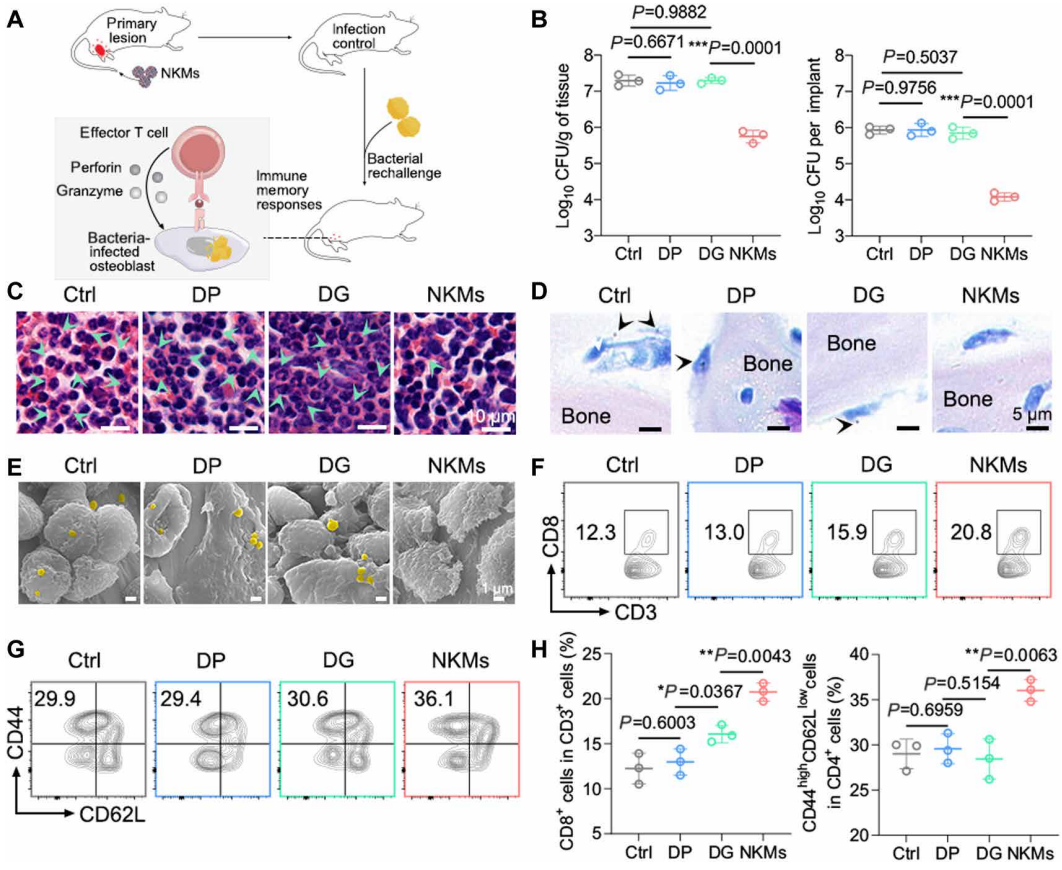

Fig. 7. Enhanced bacteria-specific immune memory responses in the presence of NKMs. (**A**) Workflow for bacterial rechallenge and immune memory responses induced by NKM treatment. (**B**) Bacterial CFU counting of infected tissues and implants 14 days after bacterial rechallenge ($n = 3$ mice). (**C** and **D**) Histology of the infected bone was evaluated by H&E (C) and Giemsa (D) staining 14 days after bacterial rechallenge. The cyan arrows indicate neutrophils, and the white arrows indicate bacteria. Scale bar, 10 μm. (**E**) Representative SEM images for infected implants from bacterial rechallenge mice. Scale bar, 1 μm. *S. aureus* is pseudocolored yellow. (**F** to **H**) The numbers of CTL ($CD3^+CD8^+$) and memory T cells ($CD4^+CD44^{high}CD62L^{low}$) were determined in the bone marrow on day 14 after bacterial rechallenge. Data in bar graphs are presented as mean ± SD ($n = 3$), and n represents independent experiments. Two-tailed Student's t test was used for statistical analysis. Exact P values were provided.

releases from the system for intracellular bacterial elimination (Fig. 4), which is in high similarity with the functions of NK cells against the intracellular bacteria (*53*). This NK cell–mimicking process results in intra-osteoblastic *S. aureus* elimination both in vitro and in vivo, while in contrast, vancomycin, the current standard of care for MRSA infection, failed to kill these bacteria (Fig. 2). Third, NKMs elevate the immunostimulating capacity of the infected osteoblast by activating NK cell–mediated cytotoxicity and T cell receptor signaling pathway, thus leading to the increased productions of immunoregulatory cytokines such as IL-6, TNF-α, and GM-CSF (Fig. 5 and fig. S8). The immunoactivated osteoblasts would recruit innate and adaptive immune cells and drive antigen-specific activation of T lymphocytes to eliminate intracellular bacterial pathogens of bone tissue (*67*, *69*, *70*).

Although intra-osteoblastic *S. aureus* has been extensively evidenced in vitro, the intracellular persistence of *S. aureus* in bone cells has rarely been validated in vivo, which challenges the development of intracellular bacteria-targeted therapeutics in chronic osteomyelitis (*75*). We collected *S. aureus*–infected bone tissue samples from clinical patients who were diagnosed with chronic *S. aureus* peri-implant infections. Multi-parameter analysis on the infected bone demonstrated that osteoblasts can be chronically infected by *S. aureus* in vivo (figs. S1 to S5). These clinical data provide strong evidence for intracellular survival of *S. aureus* in osteomyelitis, which indicates the necessity and clinical value of developing intracellular bacteria-targeted therapeutic strategies. Besides, we have also evidenced the presence of *S. aureus* in bone cells of mice femur in vivo using histological analysis and bio-TEM (Figs. 6 and 7), and found that the administration of NKMs can robustly suppress the infections in both primary mouse osteomyelitis and bacterial rechallenge settings. NKM treatment reduces both intracellular bacterial load and biofilm burden, thus restoring the homoeostasis and alleviating the tissue damage by the bacteria. Additionally, we found that NKM treatment can largely alleviate the formation of staphylococcal abscess communities and eliminate the bacteria invaded in the OLCN of bone, proving the high efficacy of NKM therapy in eliminating bacteria in the osteomyelitis model.

The intracellular location is known to be a heaven for *S. aureus* to evade and compromise host immune system (*83*). Therefore, alternative techniques of stimulating host innate immune responses would be useful in the treatment and prevention of intracellular *S. aureus* infection. We discovered that NKMs evoke antibacterial immunity by activating $CD8^+$ T cells and promoting the proliferations of NK cells (Fig. 6). $CD8^+$ T cells and NK cells are both responsible for

detecting infected cells and releasing cytotoxic granule proteins through the immune synapse between the immune cell and the infected cell (*53*, *77*). This result implies that NKMs not only can directly destroy intracellular bacteria but also evoke the antibacterial immunity of the host cells. We have also found that NKMs prevent the infection recurrence by evoking bacteria-specific T cell immunological memory responses (Fig. 7), implying the translational potential of NKMs for preventing osteomyelitis relapse.

We herein have tested the antibacterial efficacy of NKMs against intracellular *S. aureus* infection in the current study, while other kinds of prevalent human infections beyond *S. aureus*, which also rely on the similar intracellular protections like *S. aureus* in human bodies, remain to be explored in depth. Nevertheless, the present NKMs offer a paradigm of NK cell–mimicking platform to treat various intracellular infections.

MATERIALS AND METHODS

Study design

The study was designed to validate an NK cell mimic to eliminate intracellular bacteria and activate the host's immune response system for the treatment of osteomyelitis infections. In vitro characterization of formulated NKMs revealed the biological activity of the perforin and granzyme after encapsulation and released from the NKMs. Electrochemical experiments, enzyme-linked immunosorbent assay, bio-TEM, SAXS, and SEM micrographs were used to study the mechanism and behavior of NKMs during *S. aureus*–infected osteoblast-targeted degradation, perforation, and bacterial sterilization. In vivo antimicrobial efficacy of NKMs was evaluated using a previously established model of *S. aureus*–induced titanium implant osteomyelitis infection. To measure the efficacy of bacterial clearance after perforin and granzyme released from the NKM system, we used mCherry–*S. aureus* and in vivo imaging to monitor infection progression. The immunomodulatory efficacy of NKMs was assessed by flow cytometry analysis of the infected bone marrows. In addition, the antimicrobial efficacy of NKMs was determined by CFU counting, TEM, SEM, and histopathologic analysis of the infected tissues and implants. Finally, the translational potential of NKMs was assessed by analyzing the biosafety of the nanoparticles in the organs of interest. All clinical patient samples were obtained and used in accordance with the approval of the Ethics Committee of the Sixth People's Hospital, Shanghai Jiao Tong University School of Medicine [approval no. 2023-KY-017(K)]. All animal studies conformed to the guidelines by the Animal Care Ethics Commission of Shanghai Sixth People's Hospital, Shanghai Jiao Tong University School of Medicine (ethics approval number: DWLL2023-0469).

The time point of infection inoculation, treatment group size, and endpoints were selected based on previous experience with the corresponding animal models. Animals were randomly assigned to treatment and time point groups and given numerical identifiers. Experimental group size (n) is indicated in all figure legends. All experiments involving animals and biological samples were approved by the Animal Care Center and Use Committee of the Shanghai Sixth People's Hospital.

Statistical analysis

All results are presented as mean ± SD unless otherwise indicated. The significance between two groups was evaluated by two-tailed Student's t test. One-way analysis of variance (ANOVA) with Tukey's post hoc test was used for multiple comparisons. Statistical analysis was evaluated using GraphPad Prism 6.0. P values of less than 0.05 were considered significant. $^{*}P < 0.05$, $^{**}P < 0.01$, $^{***}P < 0.001$, and $^{****}P < 0.0001$.

Supplementary Materials

This PDF file includes:

Supplementary Materials and Methods
Figs. S1 to S39
Tables S1 to S3

REFERENCES AND NOTES

1. D. J. Diekema, M. A. Pfaller, F. J. Schmitz, J. Smayevsky, J. Bell, R. N. Jones, M. Beach, SENTRY Partcipants Group, Survey of infections due to Staphylococcus species: Frequency of occurrence and antimicrobial susceptibility of isolates collected in the United States, Canada, Latin America, Europe, and the Western Pacific region for the SENTRY Antimicrobial Surveillance Program, 1997-1999. *Clin. Infect. Dis.* **32**, S114–S132 (2001).
2. H. W. Boucher, G. H. Talbot, J. S. Bradley, J. E. Edwards, D. Gilbert, L. B. Rice, M. Scheld, B. Spellberg, J. Bartlett, Bad bugs, no drugs: No ESKAPE! An update from the infectious diseases society of America. *Clin. Infect. Dis.* **48**, 1–12 (2009).
3. F. Rossi, L. Diaz, A. Wollam, D. Panesso, Y. Zhou, S. Rincon, A. Narechania, G. Xing, T. S. R. di Gioia, A. Doi, T. T. Tran, J. Reyes, J. M. Munita, L. P. Carvajal, A. Hernandez-Roldan, D. Brandão, I. M. van der Heijden, B. E. Murray, P. J. Planet, G. M. Weinstock, C. A. Arias, Transferable vancomycin resistance in a community-associated MRSA lineage. *N. Engl. J. Med.* **370**, 1524–1531 (2014).
4. A. S. Lee, H. de Lencastre, J. Garau, J. Kluytmans, S. Malhotra-Kumar, A. Peschel, S. Harbarth, Methicillin-resistant *Staphylococcus aureus*. *Nat. Rev. Dis. Primers.* **4**, 18033 (2018).
5. T. Jarry, G. Memmi, A. Cheung, The expression of alpha-hemolysin is required for *Staphylococcus aureus* phagosomal escape after internalization in CFT-1 cells. *Cell. Microbiol.* **10**, 1801–1814 (2008).
6. Y.-A. Que, J. A. Haefliger, L. Piroth, P. François, E. Widmer, J. M. Entenza, B. Sinha, M. Herrmann, P. Francioli, P. Vaudaux, P. Moreillon, Fibrinogen and fibronectin binding cooperate for valve infection and invasion in *Staphylococcus aureus* experimental endocarditis. *J. Exp. Med.* **201**, 1627–1635 (2005).
7. F. Peyrusson, H. Varet, T. K. Nguyen, R. Legendre, O. Sismeiro, J. Y. Coppée, C. Wolz, T. Tenson, F. van Bambeke, Intracellular *Staphylococcus aureus* persisters upon antibiotic exposure. *Nat. Commun.* **11**, 2200 (2020).
8. M. J. Fraunholz, B. Sinha, Intracellular staphylococcus aureus: Live-in and let die. *Front. Cell. Infect. Microbiol.* **2**, 43 (2012).
9. F. A. Kapral, M. G. Shayegani, Intracellular survival of staphylococci. *J. Exp. Med.* **110**, 123–138 (1959).
10. K. Ray, B. Marteyn, P. J. Sansonetti, C. M. Tang, Life on the inside: The intracellular lifestyle of cytosolic bacteria. *Nat. Rev. Microbiol.* **7**, 333–340 (2009).
11. B. Holmes, P. G. Quie, D. B. Windhorst, B. Pollara, R. A. Good, Protection of phagocytized bacteria from the killing action of antibiotics. *Nature* **210**, 1131–1132 (1966).
12. H. D. Gresham, J. H. Lowrance, T. E. Caver, B. S. Wilson, A. L. Cheung, F. P. Lindberg, Survival of *Staphylococcus aureus* inside neutrophils contributes to infection. *J. Immunol.* **164**, 3713–3722 (2000).
13. S. D. Kobayashi, K. R. Braughton, A. M. Palazzolo-Ballance, A. D. Kennedy, E. Sampaio, E. Kristosturyan, A. R. Whitney, D. E. Sturdevant, D. W. Dorward, S. M. Holland, B. N. Kreiswirth, J. M. Musser, F. DeLeo, Rapid neutrophil destruction following phagocytosis of *Staphylococcus aureus*. *J. Innate Immun.* **2**, 560–575 (2010).
14. R. S. Flannagan, D. E. Heinrichs, Macrophage-driven nutrient delivery to phagosomal *Staphylococcus aureus* supports bacterial growth. *EMBO Rep.* **21**, e50348 (2020).
15. M. C. Greenlee-Wacker, S. Kremserová, W. M. Nauseef, Lysis of human neutrophils by community-associated methicillin-resistant *Staphylococcus aureus*. *Blood* **129**, 3237–3244 (2017).
16. E. A. Masters, B. F. Ricciardi, K. L. M. Bentley, T. F. Moriarty, E. M. Schwarz, G. Muthukrishnan, Skeletal infections: Microbial pathogenesis, immunity and clinical management. *Nat. Rev. Microbiol.* **20**, 385–400 (2022).
17. D. P. Lew, F. A. Waldvogel, Osteomyelitis. *Lancet* **364**, 369–379 (2004).
18. B. H. Kapadia, R. A. Berg, J. A. Daley, J. Fritz, A. Bhave, M. A. Mont, Periprosthetic joint infection. *Lancet* **387**, 386–394 (2016).
19. N. Kavanagh, E. J. Ryan, A. Widaa, G. Sexton, J. Fennell, S. O'Rourke, K. C. Cahill, C. J. Kearney, F. J. O'Brien, S. W. Kerrigan, Staphylococcal osteomyelitis: Disease progression, treatment challenges, and future directions. *Clin. Microbiol. Rev.* **31**, e00084-17 (2018).

20. H. Lin, C. Yang, Y. Luo, M. Ge, H. Shen, X. Zhang, J. Shi, Biomimetic nanomedicine-triggered in situ vaccination for innate and adaptive immunity activations for bacterial osteomyelitis treatment. *ACS Nano* **16**, 5943–5960 (2022).
21. S. Gao, X. Yan, G. Xie, M. Zhu, X. Ju, P. J. Stang, Y. Tian, Z. Niu, Membrane intercalation-enhanced photodynamic inactivation of bacteria by a metallacycle and TAT-decorated virus coat protein. *Proc. Natl. Acad. Sci. U.S.A.* **116**, 23437–23443 (2019).
22. J. Li, X. Liu, L. Tan, Z. Cui, X. Yang, Y. Liang, Z. Li, S. Zhu, Y. Zheng, K. W. K. Yeung, X. Wang, S. Wu, Zinc-doped Prussian blue enhances photothermal clearance of *Staphylococcus aureus* and promotes tissue repair in infected wounds. *Nat. Commun.* **10**, 4490 (2019).
23. S. J. Balin, M. Pellegrini, E. Klechevsky, S. T. Won, D. I. Weiss, A. W. Choi, J. Hakimian, J. Lu, M. T. Ochoa, B. R. Bloom, L. L. Lanier, S. Stenger, R. L. Modlin, Human antimicrobial cytotoxic T lymphocytes, defined by NK receptors and antimicrobial proteins, kill intracellular bacteria. *Sci. Immunol.* **3**, eaat7668 (2018).
24. Y. Kinjo, E. Tupin, D. Wu, M. Fujio, R. Garcia-Navarro, M. R. E. I. Benhnia, D. M. Zajonc, G. Ben-Menachem, G. D. Ainge, G. F. Painter, A. Khurana, K. Hoebe, S. M. Behar, B. Beutler, I. A. Wilson, M. Tsuji, T. J. Sellati, C. H. Wong, M. Kronenberg, Natural killer T cells recognize diacylglycerol antigens from pathogenic bacteria. *Nat. Immunol.* **7**, 978–986 (2006).
25. C. Xu, S. Hu, X. Chen, Artificial cells: From basic science to applications. *Mater. Today* **19**, 516–532 (2016).
26. Z. Xu, T. Hueckel, W. T. M. Irvine, S. Sacanna, Transmembrane transport in inorganic colloidal cell-mimics. *Nature* **597**, 220–224 (2021).
27. C. Xu, N. Martin, M. Li, S. Mann, Living material assembly of bacteriogenic protocells. *Nature* **609**, 1029–1037 (2022).
28. Y. Long, L. Li, T. Xu, X. Wu, Y. Gao, J. Huang, C. He, T. Ma, L. Ma, C. Cheng, C. Zhao, Hedgehog artificial macrophage with atomic-catalytic centers to combat Drug-resistant bacteria. *Nat. Commun.* **12**, 6143 (2021).
29. H.-K. Kwon, I. Lee, K. E. Yu, S. V. Cahill, K. D. Alder, S. Lee, C. M. Dussik, J. H. Back, J. Choi, L. Song, T. R. Kyriakides, F. Y. Lee, Dual therapeutic targeting of intra-articular inflammation and intracellular bacteria enhances chondroprotection in septic arthritis. *Sci. Adv.* **7**, eabf2665 (2021).
30. S. M. Lehar, T. Pillow, M. Xu, L. Staben, K. K. Kajihara, R. Vandlen, L. DePalatis, H. Raab, W. L. Hazenbos, J. Hiroshi Morisaki, J. Kim, S. Park, M. Darwish, B. C. Lee, H. Hernandez, K. M. Loyet, P. Lupardus, R. Fong, D. Yan, C. Chalouni, E. Luis, Y. Khalfin, E. Plise, J. Cheong, J. P. Lyssikatos, M. Strandh, K. Koefoed, P. S. Andersen, J. A. Flygare, M. Wah Tan, E. J. Brown, S. Mariathasan, Novel antibody–antibiotic conjugate eliminates intracellular *S. aureus*. *Nature* **527**, 323–328 (2015).
31. S. Bai, J. Wang, K. Yang, C. Zhou, Y. Xu, J. Song, Y. Gu, Z. Chen, M. Wang, C. Shoen, B. Andrade, M. Cynamon, K. Zhou, H. Wang, Q. Cai, E. Oldfield, S. C. Zimmerman, Y. Bai, X. Feng, A polymeric approach toward resistance-resistant antimicrobial agent with dual-selective mechanisms of action. *Sci. Adv.* **7**, eabc9917 (2021).
32. Y. Liu, P. Bai, A. K. Woischnig, G. Charpin-el Hamri, H. Ye, M. Folcher, M. Xie, N. Khanna, M. Fussenegger, Immunomimetic designer cells protect mice from MRSA infection. *Cell* **174**, 259–270.e11 (2018).
33. M. Walch, F. Dotiwala, S. Mulik, J. Thiery, T. Kirchhausen, C. Clayberger, A. M. Krensky, D. Martinvalet, J. Lieberman, Cytotoxic cells kill intracellular bacteria through granulysin-mediated delivery of granzymes. *Cell* **157**, 1309–1323 (2014).
34. Y. Tada, S. H. Spoel, K. Pajerowska-Mukhtar, Z. Mou, J. Song, C. Wang, J. Zuo, X. Dong, Plant immunity requires conformational changes of NPR1 via S-nitrosylation and thioredoxins. *Science* **321**, 952–956 (2008).
35. S. Saul, C. S. Gibhardt, B. Schmidt, A. Lis, B. Pasieka, D. Conrad, P. Jung, R. Gaupp, B. Wonnenberg, E. Diler, H. Stanisz, T. Vogt, E. C. Schwarz, M. Bischoff, M. Herrmann, T. Tschernig, R. Kappl, H. Rieger, B. A. Niemeyer, I. Bogeski, A calcium-redox feedback loop controls human monocyte immune responses: The role of ORAI Ca^{2+} channels. *Sci. Signal.* **9**, ra26 (2016).
36. L. Wang, Z. Liu, J. Wang, H. Liu, J. Wu, T. Tang, H. Li, H. Yang, L. Qin, D. Ma, J. Chen, F. Liu, P. Wang, R. Zheng, P. Song, Y. Zhou, Z. Cui, X. Wu, X. Huang, H. Liang, S. Zhang, J. Cao, C. Wu, Y. Chen, D. Su, X. Chen, G. Zeng, B. Ge, Oxidization of TGFβ-activated kinase by MPT53 is required for immunity to Mycobacterium tuberculosis. *Nat. Microbiol.* **4**, 1378–1388 (2019).
37. B. Park, S. Lee, E. Kim, K. Cho, S. R. Riddell, S. Cho, K. Ahn, Redox regulation facilitates optimal peptide selection by MHC class I during antigen processing. *Cell* **127**, 369–382 (2006).
38. L. Tang, Y. Zheng, M. B. Melo, L. Mabardi, A. P. Castaño, Y. Q. Xie, N. Li, S. B. Kudchodkar, H. C. Wong, E. K. Jeng, M. V. Maus, D. J. Irvine, Enhancing T cell therapy through TCR-signaling-responsive nanoparticle drug delivery. *Nat. Biotechnol.* **36**, 707–716 (2018).
39. S. H. Saunders, E. C. M. Tse, M. D. Yates, F. J. Otero, S. A. Trammell, E. D. A. Stemp, J. K. Barton, L. M. Tender, D. K. Newman, Extracellular DNA promotes efficient extracellular electron transfer by pyocyanin in pseudomonas aeruginosa biofilms. *Cell* **182**, 919–932. e19 (2020).
40. Y. Xu, R. Rothe, D. Voigt, S. Hauser, M. Cui, T. Miyagawa, M. Patino Gaillez, T. Kurth, M. Bornhäuser, J. Pietzsch, Y. Zhang, Convergent synthesis of diversified reversible network leads to liquid metal-containing conductive hydrogel adhesives. *Nat. Commun.* **12**, 2407 (2021).
41. D. Bar-Or, R. Bar-Or, L. T. Rael, E. N. Brody, Oxidative stress in severe acute illness. *Redox Biol.* **4**, 340–345 (2015).
42. Y. Wang, Y. Jiang, D. Wei, P. Singh, Y. Yu, T. Lee, L. Zhang, H. K. Mandl, A. S. Piotrowski-Daspit, X. Chen, F. Li, X. Li, Y. Cheng, A. Josowitz, F. Yang, Y. Zhao, F. Wang, Z. Zhao, A. Huttner, R. S. Bindra, H. Xiao, W. Mark Saltzman, Nanoparticle-mediated convection-enhanced delivery of a DNA intercalator to gliomas circumvents temozolomide resistance. *Nat. Biomed. Eng.* **5**, 1048–1058 (2021).
43. T. Kim, E. Momin, J. Choi, K. Yuan, H. Zaidi, J. Kim, M. Park, N. Lee, M. T. McMahon, A. Quinones-Hinojosa, J. W. M. Bulte, T. Hyeon, A. A. Gilad, Mesoporous silica-coated hollow manganese oxide nanoparticles as positive T1 contrast agents for labeling and mri tracking of adipose-derived mesenchymal stem cells. *J. Am. Chem. Soc.* **133**, 2955–2961 (2011).
44. D. Tarn, C. E. Ashley, M. Xue, E. C. Carnes, J. I. Zink, C. J. Brinker, Mesoporous silica nanoparticle nanocarriers: Biofunctionality and biocompatibility. *Acc. Chem. Res.* **46**, 792–801 (2013).
45. Q. Zhang, X. Wang, P. Z. Li, K. T. Nguyen, X. J. Wang, Z. Luo, H. Zhang, N. S. Tan, Y. Zhao, Biocompatible, uniform, and redispersible mesoporous silica nanoparticles for cancer-targeted drug delivery in vivo. *Adv. Funct. Mater.* **24**, 2450–2461 (2014).
46. M. H. Lee, Z. Yang, C. W. Lim, Y. H. Lee, S. Dongbang, C. Kang, J. S. Kim, Disulfide-cleavage-triggered chemosensors and their biological applications. *Chem. Rev.* **113**, 5071–5109 (2013).
47. G. Saito, J. A. Swanson, K. D. Lee, Drug delivery strategy utilizing conjugation via reversible disulfide linkages: Role and site of cellular reducing activities. *Adv. Drug Deliv. Rev.* **55**, 199–215 (2003).
48. R. Cheng, F. Feng, F. Meng, C. Deng, J. Feijen, Z. Zhong, Glutathione-responsive nano-vehicles as a promising platform for targeted intracellular drug and gene delivery. *J. Control. Release* **152**, 2–12 (2011).
49. Y. Yang, S. Bernardi, H. Song, J. Zhang, M. Yu, J. C. Reid, E. Strounina, D. J. Searles, C. Yu, Anion assisted synthesis of large pore hollow dendritic mesoporous organosilica nanoparticles: Understanding the composition gradient. *Chem. Mater.* **28**, 704–707 (2016).
50. Y. Chen, J. Shi, Chemistry of mesoporous organosilica in nanotechnology: Molecularly organic-inorganic hybridization into frameworks. *Adv. Mater.* **28**, 3235–3272 (2016).
51. J. E. Lee, N. Lee, T. Kim, J. Kim, T. Hyeon, Multifunctional mesoporous silica nanocomposite nanoparticles for theranostic applications. *Acc. Chem. Res.* **44**, 893–902 (2011).
52. B. Karimi, D. Elhamifar, J. H. Clark, A. J. Hunt, Ordered mesoporous organosilica with ionic-liquid framework: An efficient and reusable support for the palladium-catalyzed Suzuki-Miyaura coupling reaction in water. *Chem. A Eur. J.* **16**, 8047–8053 (2010).
53. A. C. Crespo, S. Mulik, F. Dotiwala, J. A. Ansara, S. Sen Santara, K. Ingersoll, C. Ovies, C. Junqueira, T. Tilburgs, J. L. Strominger, J. Lieberman, Decidual NK cells transfer granulysin to selectively kill bacteria in trophoblasts. *Cell* **182**, 1125–1139.e18 (2020).
54. E. L. McCarthy, S. J. Booker, Destruction and reformation of an iron-sulfur cluster during catalysis by lipoyl synthase. *Science* **358**, 373–377 (2017).
55. Q. Zhao, M. Wang, D. Xu, Q. Zhang, W. Liu, Metabolic coupling of two small-molecule thiols programs the biosynthesis of lincomycin A. *Nature* **518**, 115–119 (2015).
56. M. G. Lichtenheld, K. J. Olsen, P. Lu, D. M. Lowrey, A. Hameed, H. Hengartner, E. R. Podack, Structure and function of human perforin. *Nature* **335**, 448–451 (1988).
57. M. E. Ivanova, N. Lukoyanova, S. Malhotra, M. Topf, J. A. Trapani, I. Voskoboinik, H. R. Saibil, The pore conformation of lymphocyte perforin. *Sci. Adv.* **8**, eabk3147 (2022).
58. S. I. Williams, X. Yu, T. Ni, R. J. C. Gilbert, P. J. Stansfeld, Structural, functional and computational studies of membrane recognition by plasmodium perforin-like proteins 1 and 2. *J. Mol. Biol.* **434**, 167642 (2022).
59. L. Shi, D. Keefe, E. Durand, H. Feng, D. Zhang, J. Lieberman, Granzyme B binds to target cells mostly by charge and must be added at the same time as perforin to trigger apoptosis 1. *J. Immunol.* **174**, 5456–5461 (2005).
60. C. Leung, A. W. Hodel, A. J. Brennan, N. Lukoyanova, S. Tran, C. M. House, S. C. Kondos, J. C. Whisstock, M. A. Dunstone, J. A. Trapani, I. Voskoboinik, H. R. Saibil, B. W. Hoogenboom, Real-time visualization of perforin nanopore assembly. *Nat. Nanotechnol.* **12**, 467–473 (2017).
61. N. Luo, J. K. Weber, S. Wang, B. Luan, H. Yue, X. Xi, J. Du, Z. Yang, W. Wei, R. Zhou, G. Ma, PEGylated graphene oxide elicits strong immunological responses despite surface passivation. *Nat. Commun.* **8**, 14537 (2017).
62. Y. Wang, Z. Li, X. Wang, Z. Zhao, L. Jiao, R. Liu, K. Wang, R. Ma, Y. Yang, G. Chen, Y. Wang, X. Bian, Insights into membrane association of the SMP domain of extended synaptotagmin. *Nat. Commun.* **14**, 1504 (2023).
63. T. A. Fehniger, S. F. Cai, X. Cao, A. J. Bredemeyer, R. M. Presti, A. R. French, T. J. Ley, Acquisition of murine NK cell cytotoxicity requires the translation of a pre-existing pool of Granzyme B and perforin mRNAs. *Immunity* **26**, 798–811 (2007).
64. Y. Jiang, W. Zheng, K. Tran, E. Kamilar, J. Bariwal, H. Ma, H. Liang, Hydrophilic nanoparticles that kill bacteria while sparing mammalian cells reveal the antibiotic role of nanostructures. *Nat. Commun.* **13**, 197 (2022).

65. L. Yang, V. D. Gordon, D. R. Trinkle, N. W. Schmidt, M. A. Davis, C. DeVries, A. Som, J. E. Cronan Jr., G. N. Tew, G. C. L. Wong, Mechanism of a prototypical synthetic membrane-active antimicrobial: Efficient hole-punching via interaction with negative intrinsic curvature lipids. *Proc. Natl. Acad. Sci. U.S.A.* **105**, 20595–20600 (2008).
66. H. Liang, G. Whited, C. Nguyen, G. D. Stucky, The directed cooperative assembly of proteorhodopsin into 2D and 3D polarized arrays. *Proc. Natl. Acad. Sci. U.S.A.* **104**, 8212–8217 (2007).
67. I. Marriott, Osteoblast responses to bacterial pathogens: A previously unappreciated role for bone-forming cells in host defense and disease progression. *Immunol. Res.* **30**, 291–308 (2004).
68. T. Yoshimoto, M. Kittaka, A. A. P. Doan, R. Urata, M. Prideaux, R. E. Rojas, C. V. Harding, W. Henry Boom, L. F. Bonewald, E. M. Greenfield, Y. Ueki, Osteocytes directly regulate osteolysis via MYD88 signaling in bacterial bone infection. *Nat. Commun.* **13**, 6648 (2022).
69. J. Josse, F. Velard, S. C. Gangloff, *Staphylococcus aureus* vs. osteoblast: Relationship and consequences in osteomyelitis. *Front. Cell. Infect. Microbiol.* **5**, 85 (2015).
70. V. Granata, V. Possetti, R. Parente, B. Bottazzi, A. Inforzato, C. Sobacchi, The osteoblast secretome in Staphylococcus aureus osteomyelitis. *Front. Immunol.* **13**, 1048505 (2022).
71. L. Abad, J. Josse, J. Tasse, S. Lustig, T. Ferry, A. Diot, F. Laurent, F. Valour, Antibiofilm and intraosteoblastic activities of rifamycins against *Staphylococcus aureus*: Promising in vitro profile of rifabutin. *J. Antimicrob. Chemother.* **75**, 1466–1473 (2020).
72. L. Tuchscherr, M. Bischoff, S. M. Lattar, M. Noto Llana, H. Pförtner, S. Niemann, J. Geraci, H. van de Vyver, M. J. Fraunholz, A. L. Cheung, M. Herrmann, U. Völker, D. O. Sordelli, G. Peters, B. Löffler, Sigma factor SigB is crucial to mediate *staphylococcus aureus* adaptation during chronic infections. *PLOS Pathog.* **11**, e1004870 (2015).
73. K. L. de Mesy Bentley, R. Trombetta, K. Nishitani, S. N. Bello-Irizarry, M. Ninomiya, L. Zhang, H. L. Chung, J. L. McGrath, J. L. Daiss, H. A. Awad, S. L. Kates, E. M. Schwarz, Evidence of staphylococcus aureus deformation, proliferation, and migration in canaliculi of live cortical bone in murine models of osteomyelitis. *J. Bone Miner. Res.* **32**, 985–990 (2017).
74. C. W. Farnsworth, E. M. Schott, S. E. Jensen, J. Zukoski, A. M. Benvie, M. A. Refaai, S. L. Kates, E. M. Schwarz, M. J. Zuscik, S. R. Gill, R. A. Mooney, Adaptive upregulation of clumping factor A (ClfA) by staphylococcus aureus in the obese, type 2 diabetic host mediates increased virulence. *Infect. Immun.* **85**, e01005-16 (2017).
75. E. A. Masters, R. P. Trombetta, K. L. de Mesy Bentley, B. F. Boyce, A. L. Gill, S. R. Gill, K. Nishitani, M. Ishikawa, Y. Morita, H. Ito, S. N. Bello-Irizarry, M. Ninomiya, J. D. Brodell Jr., C. C. Lee, S. P. Hao, I. Oh, C. Xie, H. A. Awad, J. L. Daiss, J. R. Owen, S. L. Kates, E. M. Schwarz, G. Muthukrishnan, Evolving concepts in bone infection: Redefining "biofilm", "acute vs. chronic osteomyelitis", "the immune proteome" and "local antibiotic therapy". *Bone Res.* **7**, 20 (2019).
76. R. G. Gaudet, S. Zhu, A. Halder, B.-H. Kim, C. J. Bradfield, S. Huang, D. Xu, A. Mamińska, T. N. Nguyen, M. Lazarou, E. Karatekin, K. Gupta, J. D. M. Micking, A human apolipoprotein L with detergent-like activity kills intracellular pathogens. *Science* **373**, eabf8113 (2021).
77. C. Junqueira, C. R. R. Barbosa, P. A. C. Costa, A. Teixeira-Carvalho, G. Castro, S. Sen Santara, R. P. Barbosa, F. Dotiwala, D. B. Pereira, L. R. Antonelli, J. Lieberman, R. T. Gazzinelli, Cytotoxic $CD8^+$ T cells recognize and kill Plasmodium vivax-infected reticulocytes. *Nat. Med.* **24**, 1330–1336 (2018).
78. B. C. Young, M. Dudareva, M. P. Vicentine, A. J. Hotchen, J. Ferguson, M. McNally, Microbial persistence, replacement and local antimicrobial therapy in recurrent bone and joint infection. *Antibiotics* **12**, 708 (2023).
79. S. Krishna, J. Yang, H. Wang, Y. Qiu, X. P. Zhong, Role of tumor suppressor TSC1 in regulating antigen-specific primary and memory CD8 T cell responses to bacterial infection. *Infect. Immun.* **82**, 3045–3057 (2014).
80. C. L. Marriott, G. Carlesso, R. Herbst, D. R. Withers, ICOS is required for the generation of both central and effector $CD4^+$ memory T-cell populations following acute bacterial infection. *Eur. J. Immunol.* **45**, 1706–1715 (2015).
81. J. K. Ellington, M. Harris, L. Webb, B. Smith, T. Smith, K. Tan, M. Hudson, Intracellular *Staphylococcus aureus*. A mechanism for the indolence of osteomyelitis. *J. Bone Joint. Surg. Br.* **85**, 918–921 (2003).
82. T. J. Laskowski, A. Biederstadt, K. Rezvani, Natural killer cells in antitumour adoptive cell immunotherapy. *Nat. Rev. Cancer* **22**, 557–575 (2022).
83. I. Pastar, A. P. Sawaya, J. Marjanovic, J. L. Burgess, N. Strbo, K. E. Rivas, T. C. Wikramanayake, C. R. Head, R. C. Stone, I. Jozic, O. Stojadinovic, E. Y. Kornfeld, R. S. Kirsner, H. Lev-Tov, M. Tomic-Canic, Intracellular *Staphylococcus aureus* triggers pyroptosis and contributes to inhibition of healing due to perforin-2 suppression. *J. Clin. Invest.* **131**, e133727 (2021).

Acknowledgments

Funding: This work was supported by the National Key R&D Program of China (grant no. 2022YFB3804500 to J.S.), Shanghai Pilot Program for Basic Research-Chinese Academy of Science, Shanghai Branch (grant no. JCYJ-SHFY-2022-003 to H.L.), National Natural Science Foundation of China (grant nos. 52002391 to J.S., 82302717 to C.Y., and 52372276 to H.L.), Youth Innovation Promotion Association CAS (grant no. 2023262 to H.L.), Basic Research Program of Shanghai Municipal Government (grant no. 21JC1406000 to J.S.), CAMS Innovation Fund for Medical Sciences (grant no. 2021-I2M-5-012 to J.S.), Young Elite Scientists Sponsorship Program by CAST (grant no. YESS20210149 to H.L.), Shanghai Science and Technology Committee Rising-Star Program (grant no. 22QA1410200 to H.L.), Shanghai Sailing Program (grant no. 23YF1432200 to C.Y.), and China Postdoctoral Science Foundation (grant no. 2023M732310 to C.Y.). **Author contributions:** Conceptualization: M.G., C.Y., H.L., and J.S. Investigation: M.G., Y.-X.Z., W.W., and C.Y. Methodology: Z.R. and H.L. Data curation: M.G. Writing—original draft: M.G. Funding acquisition: C.Y. and H.L. Project administration: C.Y. Supervision: C.Y., H.L., and J.S. Writing—review and editing: C.Y., H.L., and J.S. **Competing interests:** The authors declare that they have no competing interests. **Data and materials availability:** All data needed to evaluate the conclusions in the paper are present in the paper and/or the Supplementary Materials.

Submitted 22 March 2024
Accepted 25 September 2024
Published 30 October 2024
10.1126/sciadv.adp3976